Marine and Petroleum Geology 89 (2018) 464–478

Contents lists available at ScienceDirect

Marine and Petroleum Geology

journal homepage: www.elsevier.com/locate/marpetgeo

Research paper

Enhanced structural interpretation from 3D seismic data using hybrid attributes: New insights into fault visualization and displacement in Cretaceous formations of the Scotian Basin, offshore Nova Scotia

Animesh Mandal*, Eshaan Srivastava

Department of Earth Sciences, Indian Institute of Technology, Kanpur 208016, India

ARTICLE INFO

Keywords:
Scotian Basin
3D seismic
Meta-attributes
Neural networks
Structural interpretation

ABSTRACT

Meta or hybrid attributes extracted from seismic data through artificial neural networks enhance structural details in subsurface strata. Cretaceous units within the Penobscot prospect are devoid of such interpretations. Although these units are plausible zones for hydrocarbon generation and accumulation, the role of geologic structures responsible for such entrapment is poorly understood. The present study enlightens these latter geological structures through a case study that uses 3D time-migrated seismic data from the Penobscot prospect in the Scotian Basin. A modern data conditioning approach, used together with multi-attribute analyses and a supervised neural network, have brought out the minute details of subsurface geologic structures through a hybrid attribute, called the fault probability cube (FPC). The present fault displacement analysis reveals that the major fault of the prospect has evolved by the coalescence of different fault segments grown over space and time, and has demonstrated a predominant NNW-SSE structural trend. Such a geometry has structurally modulated the Cretaceous units (the Logan Canyon, the Dawson Canyon and the Wyandot Formations) giving rise to different horst-graben structures and fracture networks, as shown by the FPC attribute. This generates complicated structural deformation and accommodation space, thereby enabling different trapping zones for hydrocarbon accumulation within these units. Such a detailed structural understanding will provide significant input to the future exploration and development programme in the Penobscot prospect.

1. Introduction

Structural interpretation of seismic data helps to decipher the architecture of subsurface strata by imaging minute details of geologic structures, e.g. faults, folds, fracture networks etc. Thereby, it sheds light over the architecture of hydrocarbon-bearing beds. Interpreters very often encounter major challenges when obtaining accurate images of these geologic structures from geophysical data. However, several advancements have recently occurred in interpretation techniques to overcome such challenges. Over the past few decades, seismic attributes have played a key role in adding value to such interpretation techniques. Several authors (e.g. Bahorich and Farmer, 1995; Tingdahl and de Groot, 2003; Al-Dossary and Marfurt, 2006; Cohen et al., 2006; Chopra and Marfurt, 2007a, b; Hale, 2013; Marfurt and Alves, 2015; Iacopini et al., 2016; Kumar, 2016, Di and Gao, 2017) have documented the usefulness of structural attributes for the detailed structural interpretation of seismic data. Recent advances in attribute analysis techniques such as multi-attribute analyses through artificial neural networks (ANNs) have gained a wide range of acceptance due to their efficient imaging of lithological and structural units (McCormack, 1991; Meldahl et al., 1999; Ligtenberg and Wansink, 2001; Tingdahl and de Rooij, 2005; Smith and Treitel, 2010; Zheng et al., 2014; Singh et al., 2016; Kumar and Mandal, 2017). However, extraction of enhanced subsurface images from seismic data is still a challenging task, making it as one of the most active research area in seismic interpretation. There always exists scope for improvement in the computation of these attributes, as well as logically combining them to extract an enhanced and robust subsurface image.

The present study is focused on identifying and imaging detailed structural features, e.g. faults, fracture networks, etc. observed within Cretaceous strata (namely the Logan Canyon, the Dawson Canyon and Wyandot Formations) in the Penobscot prospect, SW of mainland Nova Scotia (Fig. 1a). The literature pertaining to the study area (Kettanah, 2013; Campbell et al., 2015; Qayyum et al., 2015; Yagci, 2016) demonstrates the presence of over-pressured intervals, deep-seated structures, regularly spaced oceanic fractured zones, turbiditic deposits, fault bounded roll-over anticlines, growth faults and salt diapirs that may act as potential hydrocarbon trapping zones. Kettanah (2013)

* Corresponding author.
E-mail addresses: animeshm@iitk.ac.in (A. Mandal), eshaan0304@gmail.com (E. Srivastava).

http://dx.doi.org/10.1016/j.marpetgeo.2017.10.013
Received 1 May 2017; Received in revised form 13 October 2017; Accepted 14 October 2017
Available online 21 October 2017
0264-8172/ © 2017 Elsevier Ltd. All rights reserved.

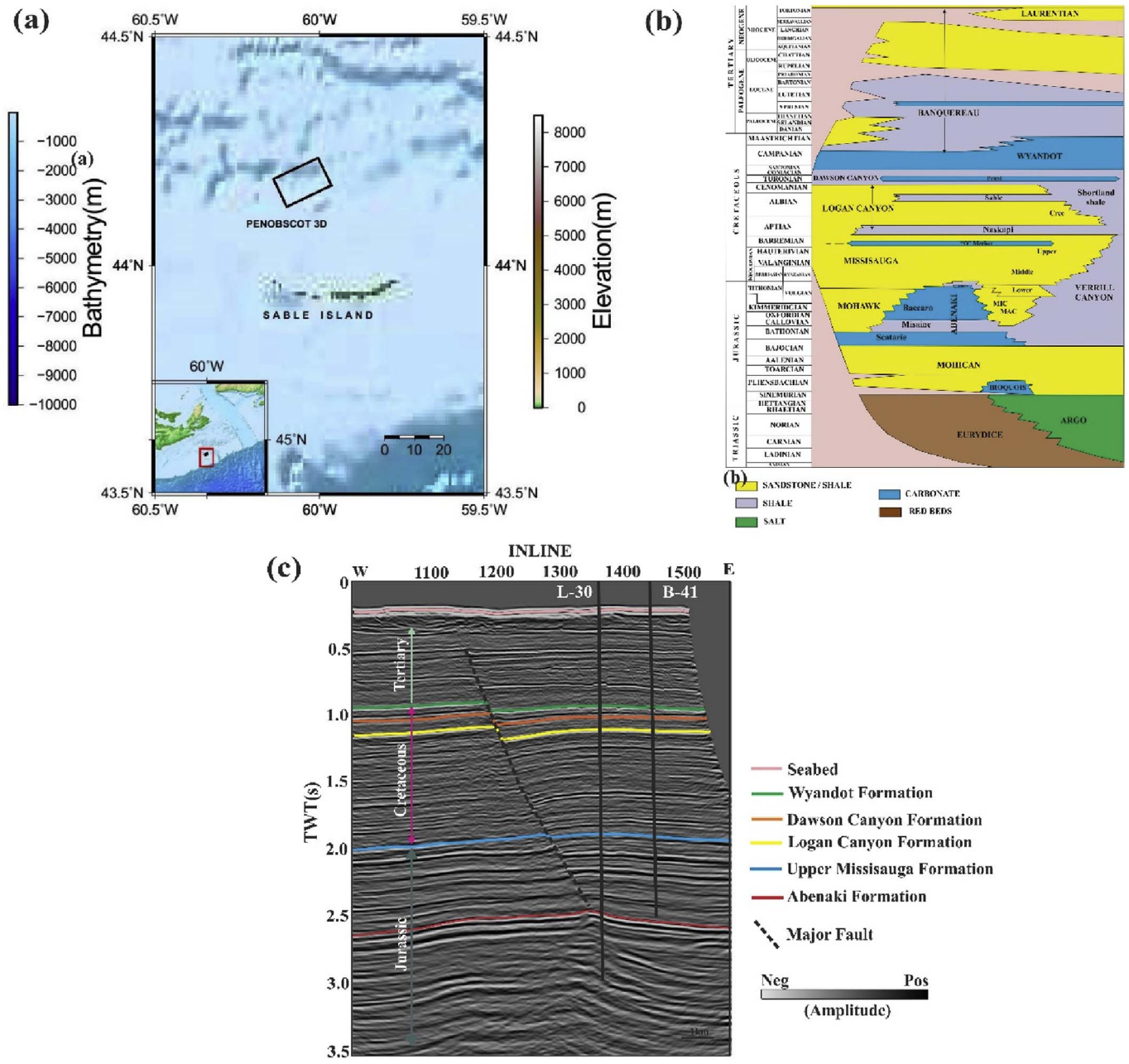

Fig. 1. (a) Location of the Penobscot 3D prospect (black rectangle), covering an area of 66.5 km^2 in the Scotian Basin off Nova Scotia. (b) Lithostratigraphy map of the Scotian Basin (after Fensome et al., 2008). c) Interpreted section for the seismic cross-line 1153 of the Penobscot prospect after tying it to well L-30 (as L-30 intersects with cross-line 1153) (See Fig. 5 for well-to-seismic tie). Different geologic strata as deposited from the Jurassic through the Cretaceous to the Tertiary are illustrated using different colours. This representation provides a validation of the interpreted horizons with the well stratigraphy of the prospect. The major fault is marked with dotted black line. (For interpretation of the references to colour in this figure legend, the reader is referred to the web version of this article.)

carried out studies on hydrocarbon fluid inclusions hosted in the evaporites of the Argo Formation to understand the probable distribution of the source rock. Qayyum et al. (2015) used the regional 2D and detailed 3D seismic data of the Scotian Shelf to understand the depositional history of Mesozoic carbonate systems (i.e. the Abenaki Formation) that are separated from overlying and underlying siliciclastic systems. Campbell et al. (2015) carried out inversion studies using 3D seismic data to identify and map subsurface lithology. In parallel, Yagci (2016) imaged a major fault system using 2D seismic data from the Penobscot prospect and seismic attributes such as instantaneous phase and variance.

Most of published work have used 2D/3D seismic data to characterize the subsurface lithology, distribution of depositional units, and major subsurface structural features offshore Nova Scotia. However, their interpretation is mostly based on one or two attributes without applying any robust data conditioning techniques to enhance signal-to-noise ratio. Also, none of them have discussed the role of geologic structures in controlling subsurface lithology. Structural details of subsurface rocks are also poorly studied within the Cretaceous units of Nova Scotia, even though hydrocarbon generation (within the Logan Canyon and Dawson Canyon Formations, as they are predominantly composed of shale) and accumulations (within the Wyandot Formation, as a bioturbated chalky horizon) has been reported for this same region (Campbell et al., 2015). In addition, the growth and evolution of structural features, as well as their importance to the evolution and hydrocarbon accumulations off Nova Scotia, were not properly

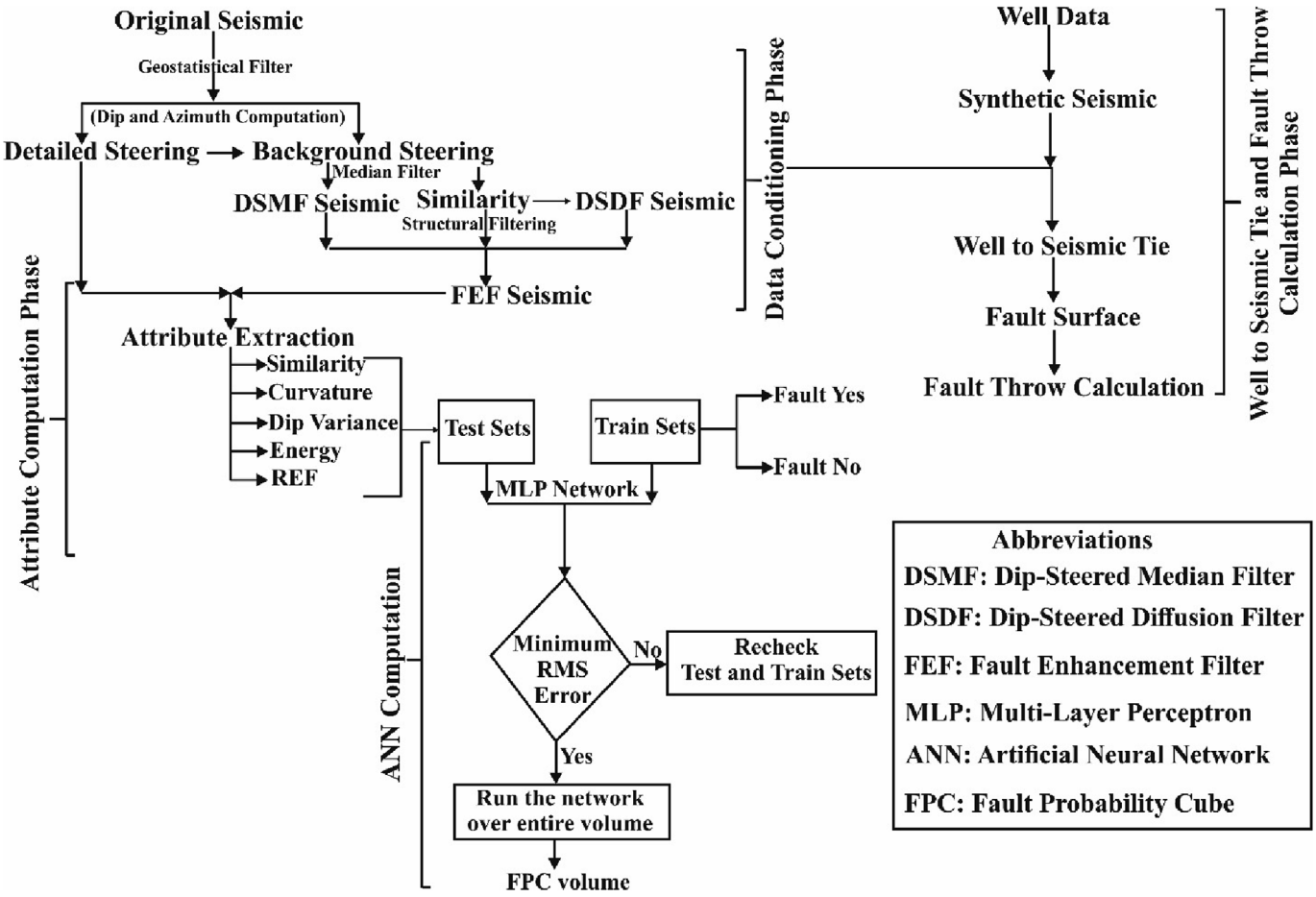

Fig. 2. Workflow adopted for the present study. It consists of four phases: data conditioning, well-to-seismic tie and fault throw calculation, attribute extraction, and neural computation.

investigated in the published literature. The present case study critically examines these facts and brings out an enhanced interpretation of subsurface structures developed within the Penobscot prospect (in general) and Cretaceous strata (in particular).

In the present study, seismic data is conditioned to improve its quality. This conditioned data volume is utilised to extract several structural attributes, which are further combined through a multi-layer perceptron network (MLP) to provide a hybrid attribute named fault probability cube (FPC). This cube stores minute details of subsurface structures and delivers an enhanced geological interpretation based on seismic data. Such an approach not only deciphers the detailed structural arrangements of subsurface geologic strata, but also complements fault displacement analyses for major faults. This approach helps in inferring the growth and evolution of faults, as well as of the adjacent geologic strata over a large geological time period. Ultimately, our approach helps defining present and future prospects within Cretaceous units off Nova Scotia.

2. Geology and tectonics

The Scotian Basin covers an area of 300,000 km^2 with sediment depth reaching up to 18 km. It comprises of several interconnected Mesozoic-Cenozoic sediment depocenters, e.g. Shelburne, Sable, Abenaki, Laurentian and South Whale sub-basins, and Orpheus graben (Wade and MacLean, 1990; Albertz et al., 2010; Kettanah, 2013). These depocenters lie over the Lower Palaeozoic basement rocks. Several authors have presented detailed accounts of the geology of the basin (Wade and MacLean, 1990; Grist et al., 1992; Wade et al., 1995; Albertz and Beaumont, 2010; Kettanah, 2013; Campbell et al., 2015). However, a brief overview of Cretaceous units in the study area is described below for completeness.

In the study area, several subsurface geologic features, e.g. grabens, half-grabens, horst structures and regularly spaced fractured zones, were developed after the break-up of Pangea as a result of varied degree of tectonic activities. This led to complex sedimentation in the study area from the Triassic period to the present day (McIver, 1972; Jansa and Wade, 1975; Grist et al., 1992; Albertz et al., 2010) (Fig. 1b). The Jurassic-Cretaceous boundary witnessed a major marine regressive phase. Such an activity resulted in the progradation and deposition of thick alluvial plain and deltaic sediments of the Mississauga Formation during the Early Cretaceous. Furthermore, the entire Cretaceous phase witnessed the deposition of sandstones, shale units, marls and chalky carbonates, a process resulting in the generation of the Logan Canyon Formation (LCF), the Dawson Canyon Formation (DCF) and the Wyandot Formation (WF) (McIver, 1972; King et al., 1974). These formation tops are shown in the seismic section in Fig. 1c after the available wells were tied to the interpreted seismic data (details are given in sub-section '4.2. Well-to-seismic ties and fault-throw calculations').

The LCF belongs to the Nova Scotia Group (McIver, 1972; King et al., 1974) and consists of a terrigenous clastic sequence of alternating sandstone and shale units. This sequence is mainly deposited along the eastern Nova Scotia Shelf. McIver (1972) reported that first lower half of the LCF consists of fine-grained, moderate to well-sorted argillaceous sandstone deposits. However, towards the base of the LCF these deposits tend to be coarser. The DCF belongs to the Gully Group (McIver, 1972; King et al., 1974) and mainly consists of marine shale deposits extending across the entire width of the Scotian Shelf (Wade et al., 1995). The DCF is calcareous or marly towards the top, finning downwards into shaley units to become silty towards its base (McIver,

1972). Burrowing and fossil debris are common throughout the unit. The WF also belongs to the Gully Group (McIver, 1972; King et al., 1974) and is the most distinctive and recognized lithologic unit deposited on the Scotian Shelf. It consists of chalky carbonates grading from pure chalk to marl.

3. The data

We have used 3D time-migrated seismic data comprising 600 inlines (Line no. 1000 to 1600) and 481 cross-lines (Line no. 1000 to 1481) over the Penobscot prospect of the Scotian Basin. The prospect lies in the transition zone from the western end of the Abenaki sub-basin to the northern updip flank of the Sable sub-basin, and is situated about 25 km NW off Sable Island (Fig. 1a). The seismic data covers an area of 66 km^2 and was acquired in a 12.5 m by 25 m (inline by cross-line) bin size with 60-fold coverage and a 2 ms sampling rate. The prospect area was drilled by two wells: Petro-Canada/Shell Penobscot L-30 drilled to a depth of 4237 m, and Petro-Canada/Shell Penobscot B-41 drilled to a depth of 3414 m (CNSOPB, 2008).

4. Methodology

The methodology adopted for the present study is illustrated in the workflow in Fig. 2. We have followed a systematic approach to attain our objectives. The entire workflow can broadly be divided into four parts: 1) data conditioning, 2) well-to-seismic ties and fault throw calculations, 3) attribute extraction, and 4) neural computation.

4.1. Data conditioning

Geologic features on the seismic data are prone to acoustic disturbances that mask their effective visualization. This also leads to a degradation of data quality, making very tiresome the task to effectively map them (Alves et al., 2015; Marfurt and Alves, 2015). Thus, to overcome such difficulties the data should be optimally conditioned such that unwanted (noisy) information is suppressed and signal quality is enhanced. We have systematically applied multiple filtering approaches to optimally remove unwanted noise from the interpreted seismic data.

The 3D time-migrated seismic data was first checked for artefacts and noise that may not be removed (or may be introduced) during the processing stage, e.g. acquisition footprints, processing artefacts, etc. (Fig. 3a, strong linear stripes along the cross-line direction). A semi-automated geostatistical filtering based on a factorial kriging technique (Magneron and Petit, 2008; Raya and Li, 2008; Magneron et al., 2009; Piazza et al., 2015) was applied in a second stage to remove these latter artefacts from the 3D seismic volume (Fig. 3b). This noise-free data (Figs. 3b and 4a) was then used for further processing.

4.1.1. Dip-azimuth computation

In the following step of the data conditioning procedure, a dip-azimuth volume (steering cube) was computed. The steering cube is prepared by extracting dip and azimuth values along the events we seek to detect (Tingdahl, 1999; Tingdahl et al., 2001; Tingdahl and de Rooij, 2005). In this process, honouring our objectives, two different steering cubes are generated: (1) the detailed steering cube (using a mild filtering step-out as: inline/cross-line/sample: 1/1/3) that preserves every minute variations in seismic reflection from the data; and (2) the background steering cube (using coarser filtering step-out as: inline/cross-line/sample: 5/5/5) that stores the overall trend of these same variations (Kumar, 2016; Kumar and Mandal, 2017). The background steering cube is used further as an input for the structural conditioning of seismic data.

4.1.2. Structural filtering

Structural conditioning of the denoised seismic data (Fig. 4a) is performed so to improve signal quality by suppressing random noise from the data. This further enhances the lateral continuity of the seismic reflections and the sharpness the geologic features imaged by the data. This is done by using a set of structure-oriented filters (SOF) (Fehmers and Höcker, 2003). These filters initially smoothen the seismic reflections, enhance their edges, and preserve all their structural characteristics.

At first, a statistical filter known as the dip-steered median filter (DSMF) is applied over the original data using the pre-processed steering cube (Chopra and Marfurt, 2007a, b; Liu et al., 2008). This results in a smoothed seismic volume called the DSMF seismic volume (Fig. 4b) that preserves the lateral continuity of seismic reflections within the data volume. Once the reflections are smoothed, an intermediate filter named dip-steered diffusion filter (DSDF) (Weickert, 1999) is used to enhance and sharpen the edges of the seismic reflections. This filter evaluates the quality of the seismic data in a dip-steered circle, and replaces the central amplitude by the amplitude where the quality is deemed the best. The filter outputs a seismic volume known as DSDF seismic volume. Both of these seismic volumes are then logically combined with a pre-computed similarity attribute using a threshold value (0.6 for this study) to process through the fault enhancement filter (FEF). This filter takes the outputs as DSMF when the similarity is high enough (higher than a threshold value); otherwise, the DSDF is used. The final output is then called as FEF seismic volume (Fig. 4c) that enhances the sharpness of the discontinuous features as present in the data by reducing the random noise. The FEF seismic volume, together with the pre-computed detailed steering cube, are then taken as inputs for extracting reliable structural attributes.

4.2. Well-to-seismic ties and fault-throw calculations

Before further processing, the denoised original and FEF seismic data are tied to the available wells in order to remove mismatches between the time and depth domains, and to relate the horizon tops with specific reflections on the seismic sections. This will ultimately help to define the horizon surface for structural interpretation. This well-to-seismic tie has been carried out by extracting a statistical wavelet of 120 ms from the reference seismic volume within a time range from 0 to 1500 ms. Based on the available density and sonic logs of the wells, acoustic impedance and reflectivity logs are computed and then convolved with the extracted wavelet to generate synthetic seismic traces. The synthetics are then compared with composite seismic traces extracted from the seismic data nearer to the well locations. In this process, a tie is attempted between the interpreted reflections from the seismic volume and those of the corresponding geological markers in the wells. During this tie, the best cross-correlation coefficient values obtained were 0.77 between the Wyandot and Dawson Formations, 0.92 between Dawson to Logan Formations, and 0.84 between Wyandot and Logan Formations for well L-30 (Fig. 5). Once the seismic data is successfully tied with the well, the geological formation tops can be shown in the seismic section (Fig. 1c) or can be picked from the entire seismic volume for further processing/interpretation.

In the present study, well tied FEF data has been utilised to measure the throw or displacement. Throw acts as an approximation for real displacement (McLeod et al., 2000; Walsh et al., 2002) of faults from the fault surface generated by auto tracking the major fault. The computed throw or displacement values were then plotted against distance and time, corresponding to the geologic strata. According to the composition of each Cretaceous unit the average P-wave velocity (Sand-shale units of LCF: 2400 m/s, Marine shale units of DCF: 2600 m/s and bioturbated chalks of WF: 2200 m/s [Avseth et al., 2005]) has been utilised to convert the observed throw values (in ms) into meters.

4.3. Seismic attribute extraction

Structural or geometric attributes play a crucial role in imaging

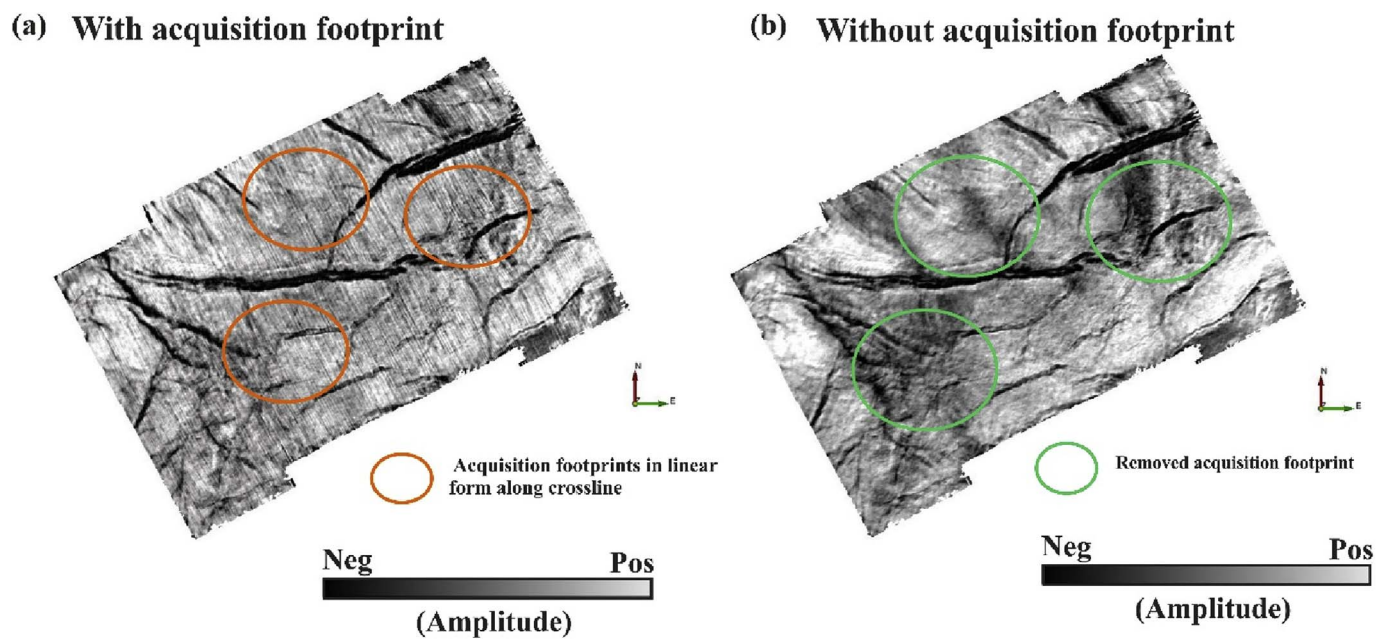

Fig. 3. Time-migrated original seismic data displayed over the Wyandot Formation. (a) Without geostatistical filtering data shows strong acquisition footprint (stripes parallel to cross-line direction), (b) With geostatistical filtering (based on factorial kriging technique) no acquisition footprints are observed in the filtered data.

complex as well as detailed geologic structures from seismic data. A brief overview of the set of geometric attributes that have been used for this study along with their extraction procedures are described in the following sections. In the present study, the attributes are initially defined using different parameters, e.g. time gates, inline/cross-line step-outs, threshold values etc., and then quality-checked over few seismic lines. Once the results are found to be satisfactory, the attributes are computed over the entire seismic volume.

4.3.1. Similarity

Similarity is a form of "coherency" that expresses how much two or more trace segments look alike (Tingdahl and de Groot, 2003). The similarity between traces or waveforms can be estimated along a reflection by computing the Euclidean distance between the amplitude vectors of the trace or waveform. When similarity attribute is computed using dip-steering as an input, the output is called the dip-steered similarity. The dip-steered similarity between two trace segments at (x_A, y_A) and (x_B, y_B), centred at the time t, is expressed as (Tingdahl, 2003; Tingdahl and de Rooij, 2005):

$$S_{dip} = 1 - \frac{|a_{dip} - b_{dip}|}{|a_{dip}| + |b_{dip}|} \quad (1)$$

where: $a_{dip} = \begin{bmatrix} u(x_A, y_A, t_A + t_1) \\ u(x_A, y_A, t_A + t_1+dt) \\ \cdots \\ u(x_A, y_A, t_A + t_2-dt) \\ u(x_A, y_A, t_A + t_2) \end{bmatrix}$, $b_{dip} = \begin{bmatrix} u(x_B, y_B, t_B + t_1) \\ u(x_B, y_B, t_B + t_1+dt) \\ \cdots \\ u(x_B, y_B, t_B + t_2-dt) \\ u(x_B, y_B, t_B + t_2) \end{bmatrix}$,

where dt is the sampling interval, t_1 is the relative start time of the comparison window, t_2 is the relative stop-time of the comparison window, t_A and t_B are the dip-steered times going from the position (x, y, t) to the traces at (x_A, y_A) and (x_B, y_B), respectively, and u is the amplitude value in the seismic data cube. This attribute varies between 0 and 1, i.e. a similarity of 1 means the trace segments are completely identical in amplitude and waveform, whereas a similarity of 0 means the trace segments are phase rotated by 180°. Thus, this similarity attribute helps immensely in delineating faults and fracture networks, as they are the locations of dissimilar trace segments.

The dip-steered similarity attribute is extracted using original seismic, dip-steered seismic and fault enhanced seismic data volumes with different vertical time windows, such as 48 ms (mid window) and 64 ms (long window), to effectively capture the effect of fault signatures throughout the data length (Fig. 6a).

4.3.2. Dip variance

Geologic structures or discontinuous features often exhibit significant changes in dip which can effectively be captured by computing the statistical variance of the dip of the seismic reflectors (Tingdahl, 2003; Tingdahl and de Rooij, 2005). The dip variance is expressed as:

$$\mathrm{var}(p_x) = \frac{1}{n-1} \sum_{\beta=-x_s}^{x_s} \sum_{\alpha=-y_s}^{y_s} \sum_{\tau=t_1}^{t_2} (p_x(x+\alpha, y+\beta, t+\tau) - \overline{p_x})^2 \quad (2)$$

Where, $\overline{p_x} = \left(\sum_{\beta=-x_s}^{x_s} \sum_{\alpha=-y_s}^{y_s} \sum_{\tau=t_1}^{t_2} p_x(x+\alpha, y+\beta, t+\tau) \right)/n$, and t_1 is the relative start-time of the sub-cube, t_2 is the relative stop-time, n is the total number of samples in the sub-cube and x_s and y_s are the sub-cubes lateral step-out in x and y direction, respectively. The above equation outputs the dip variance in the x direction. Similarly, the dip variance in the y direction $\mathrm{var}(p_y)$ can be calculated. The overall dip variance is then calculated by averaging the $\mathrm{var}(p_x)$ and $\mathrm{var}(p_y)$, and is expressed as:

$$\overline{p_{var}} = \frac{\mathrm{var}(p_x) + \mathrm{var}(p_y)}{2} \quad (2a)$$

In this study, the dip variance (Fig. 6b) is estimated taking the steering data and dip angle attributes as inputs.

4.3.3. Curvature

Curvature is a measure of the angle of a surface at a particular point (Roberts, 2001), i.e. how much a curve deviates from a straight line. It relies on geometrical deformation but not on amplitude variations. Curvature attribute is very effective in mapping minute discontinuous variations within the data (Chopra and Marfurt, 2007a, b). In the present study, we have made use of most positive volumetric curvature for interpreting subsurface structural features (Fig. 6c). The most positive curvature attribute returns positive curvature values at various points along the interpreted horizons. This attribute primarily helps in amplifying adjacent the folds and the upthrow parts of the faults.

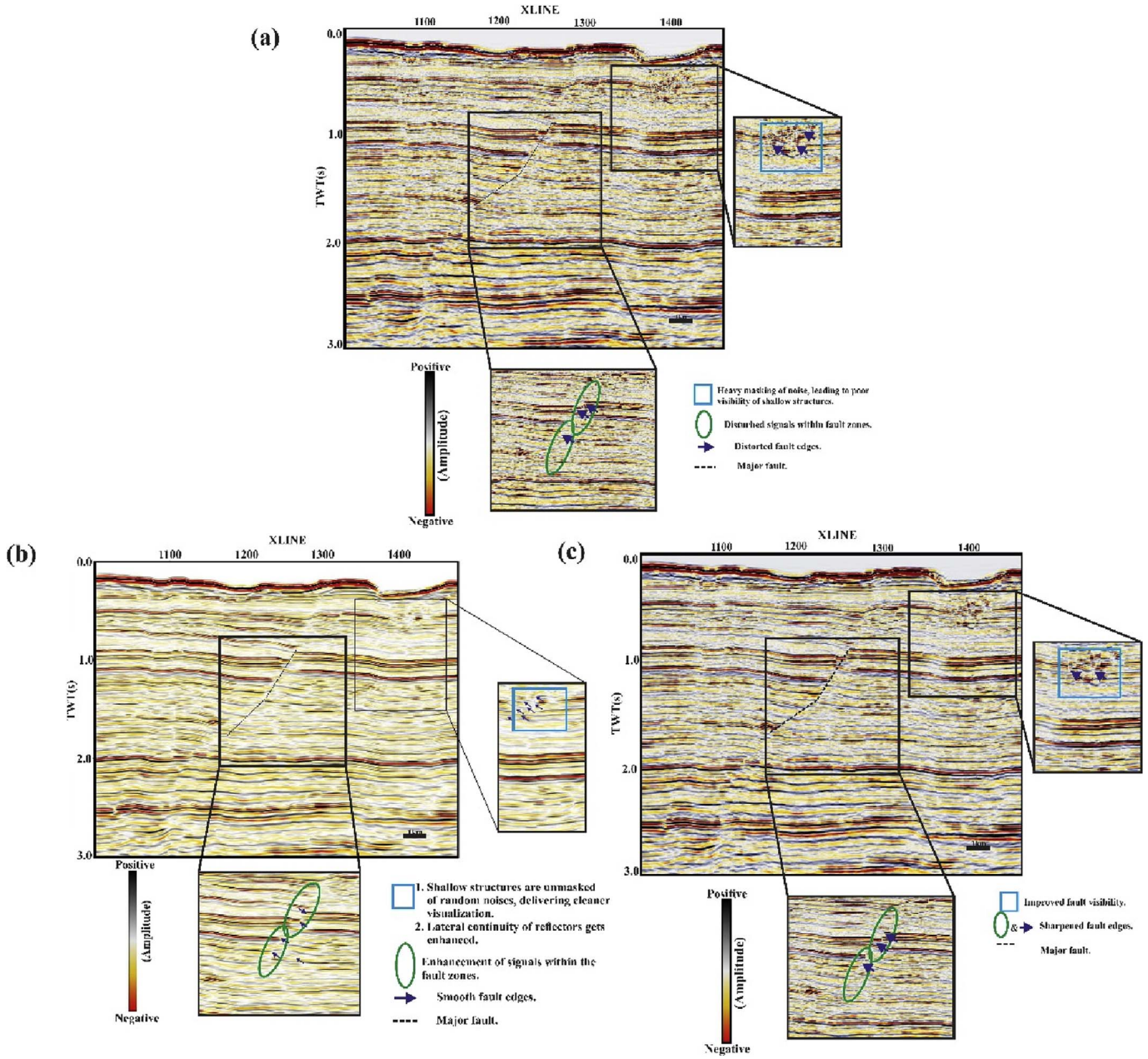

Fig. 4. (a) Original time-migrated section (after removing acquisition footprint) of seismic inline 1300 from the Penobscot 3D seismic volume. Noisy reflections observed within the shallow portion are indicated by sky blue square box. Disturbed signals within fault zones are indicated using green ovals and blue arrows. The major fault is marked using black dotted lines. (b) DSMF conditioned seismic section for the same inline. The section illustrates signal enhancement and delivers clear visualization of geologic structures. Lateral continuity of the seismic events is also improved. These observations are highlighted using a sky blue box. Reflection edges within faults are smoothened and are indicated using green ovals and blue arrows. (c) FEF seismic section for the same inline. Improved fault visibility and sharpened fault edges are highlighted by the sky blue box, green ovals and blue arrows. (For interpretation of the references to colour in this figure legend, the reader is referred to the web version of this article.)

4.3.4. Energy

Faults and fractures are also characterized by their low-amplitude and as low-energy disturbed events. The energy attribute at (x, y, and t) is defined as the sum of the squared amplitudes within a given window (Tingdahl, 2003) and is expressed as:

$$E = \sum_{\tau=t_1}^{t_2} u(x,y,t+\tau)^2 \quad (3)$$

where t_1 and t_2 are signified as the relative start and stop points of the energy window.

4.3.5. Ridge enhancement filter (REF)

REF is a hybrid attribute created by the combination of two attributes, namely the similarity and FEF seismic. The filter computes nine similarity attributes surrounding an evaluation point, and then scans it in four different directions to find the largest ridge value (Chehrazi et al., 2013). The four directions are inline, crossline and the two diagonal directions (45 and 135°) in a time slice domain of a similarity attribute volume.

$$\text{Ridge}_{i,j} = \max\left(\frac{(\text{Similarity}_{i+1,j} + \text{Similarity}_{i-1,j})}{2}\right) - \text{Similarity}_{i,j} \quad (4)$$

This equation generates ridge values at the centre point (*i*, *j*) and in the cross-line direction, where *i* and *j* represent the inline and cross-line values. The same process is repeated for the other three directions, i.e. inline and the two diagonal directions. The equation tends to give smaller values for most of the points but when a fault is crossed there

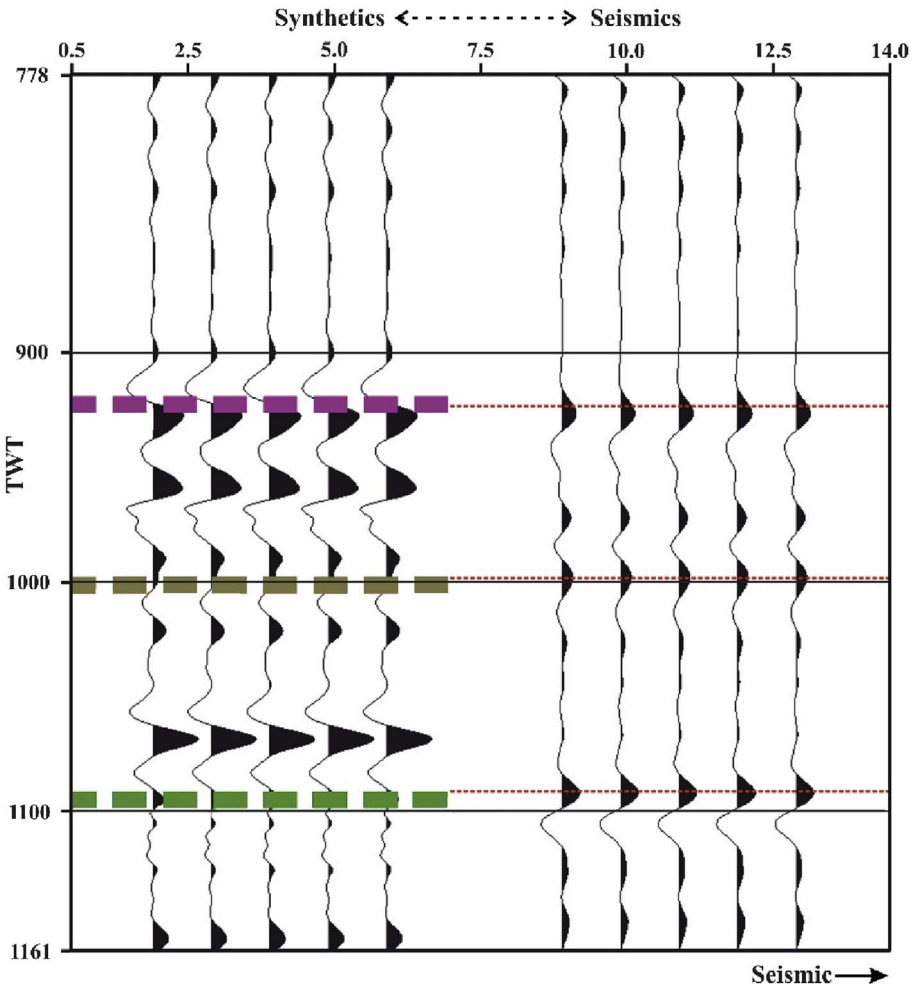

Fig. 5. Well-to-seismic tie for well L-30. The well lithologic-markers, i.e. Logan, Dawson and Wyandot Formations are represented by green, grey and pink dotted lines, respectively. The sonic and density logs of the nearby well (L-30) are convolved with extracted wavelet (120 ms) to obtain the synthetics such that reasonable correlation to the seismic could be achieved. (For interpretation of the references to colour in this figure legend, the reader is referred to the web version of this article.)

will be a large value due to the presence of large ridge perpendicular to the fault direction. This largest value will be stored as the ridge enhancement attribute. This REF attribute (Fig. 6d) not only sharpens the edges of the faults and fracture networks but also restores the connectivity of the fault systems which were previously masked by the noise (Fig. 6a).

4.4. Neural computation

The neural computation is performed on the basis of following three principles: (a) selection of input (test) data sets, (b) selection of output (trained) data sets, and (c) network operation and validation.

4.4.1. Selection of input (test) data sets

In this computation, seismic attributes act as test data sets. Geologic features are generally associated with bed (reflector) terminations, abrupt changes in dip and orientations of reflectors and loss in signal amplitude. Hence, it is very much essential to select the attributes that can effectively capture these variations and help the network to obtain an optimum output. This fact makes us to select such attributes (as discussed above in section '4.3. Seismic attribute extraction') that can provide maximum contribution for obtaining a reliable definition of geologic features from the data. These attributes are initially tested for their efficacy in capturing structural variations from the seismic data. When found suitable after several quality checks, they are finally grouped into input sets that can readily be fed into the neural network for computation.

4.4.2. Selection of training data sets

Once the input (test) data sets are prepared then the network undergoes a training schedule to produce an optimum output. Thus, the training data sets (also known as example sets) are required to train the network so that the network learns through these examples. In-order to achieve this, 200 example sets (fault and no-fault locations) are manually picked from the 1300 inline section. Fault locations are those associated with reflection terminations that are characterized by low similarity, variable dip, low energy, and frequency-loss properties. However, non-fault locations are devoid of such characteristic features.

4.4.3. Network operation and validation

A non-linear neural network is adopted for this study, and distinctively consists of three different layers; (1) the input layer, (2) the hidden layer, and (3) the output layer. These layers are interconnected with each other, making the network as a fully connected MLP network. A specific percentage of data (for the present study 30%) is used for testing the network and the rest is used for training purposes. The training set is used to update the weights of the network, while the test set is passed through the network to check the performance and avoid over-fitting. An iterative training procedure is adopted to alleviate such problems (Atakulreka and Sutivong, 2007; Singh et al., 2016; Kumar and Mandal, 2017). Training is continued until a minimum error is established between the train and test data sets. Once this is achieved, the training is stopped and the result is quality-checked over a few seismic lines. The result is then applied over the entire seismic volume to obtain a fault probability cube (FPC). This probability cube contains sample values ranging from 0 to 1, where 0 and 1 represents the lowest

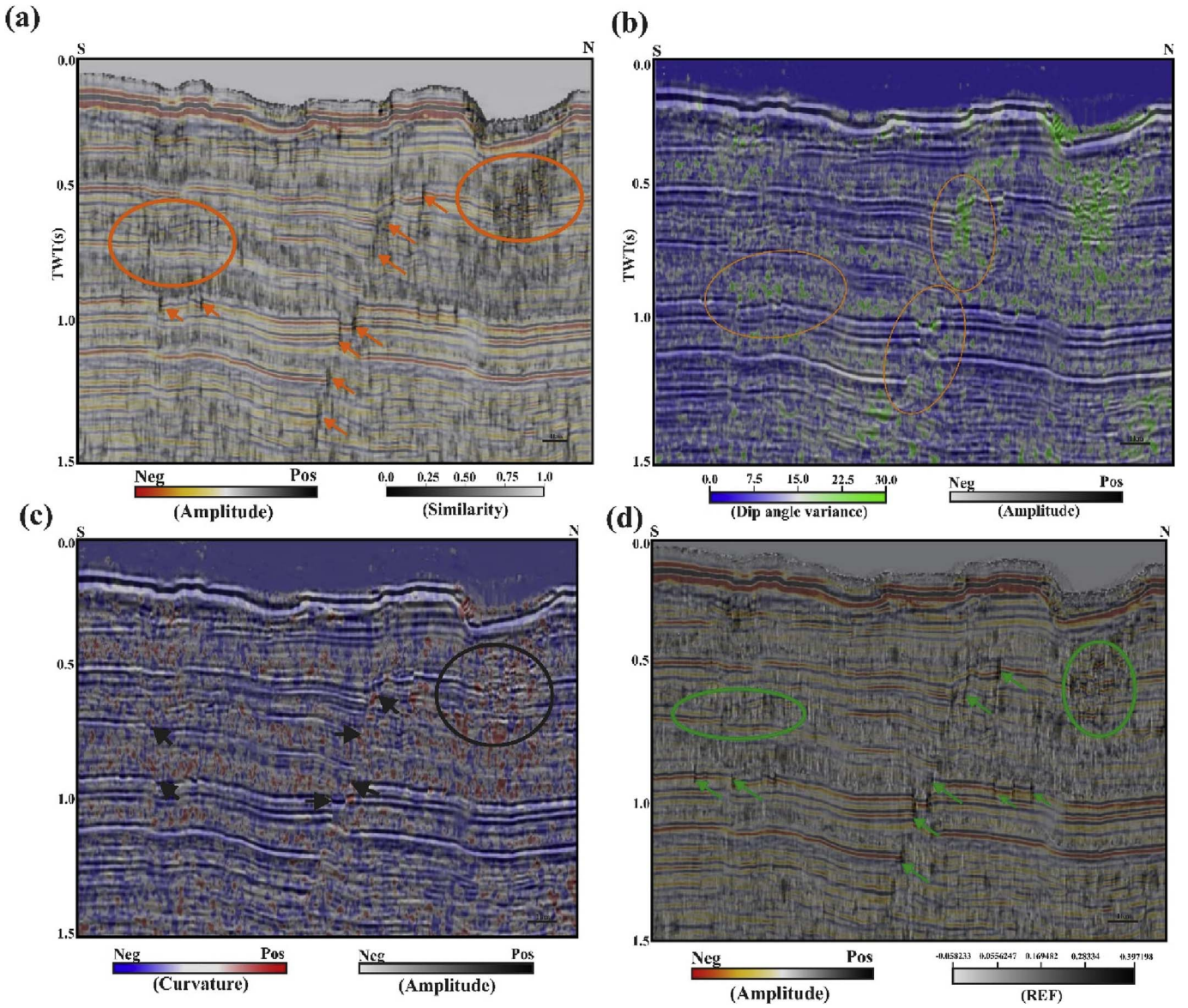

Fig. 6. (a) Co-rendered similarity attribute and amplitude data in vertical seismic section for inline 1300. The faults and discontinuities (orange ovals and arrows) are characterized with low similar values. (b) Co-rendered dip-variance attribute and amplitude data in vertical seismic section for inline 1300. Faults and discontinuities are characterized with high to low change in dip (orange ovals). (c) Co-rendered curvature attribute and amplitude data in vertical seismic section for inline 1300. Most of the upthrow portion of the faults and minute structural discontinuities are illuminated by high positive curvature values (black oval and arrows). (d) Co-rendered REF and amplitude data in vertical seismic section for inline 1300. Faults and discontinuous anomalies are associated with high ridge values and delivers a sharper contrast (green oval and arrows) in caparison to the similarity attribute (see Fig. 6a). (For interpretation of the references to colour in this figure legend, the reader is referred to the web version of this article.)

and highest probability of faults. The FPC is validated by comparing the output with the available geology of the prospect area.

5. Results

The present approach has effectively brought out the detailed signatures of the faults and discontinuous features from the seismic data. This has been demonstrated step-by-step from data conditioning to multi-attribute analysis. The unwanted acquisition footprints are effectively removed from the data at the beginning of the data conditioning stage (compare Fig. 3a–b). This helps enhancing the efficacy of FEF as reflected by the sharp visibility of faults and discontinuities that were previously masked by noise (compare Fig. 4a, 4b and 4c, particularly the zoomed rectangular and oval parts). Hence, this enhanced FEF data provides more confidence when extracting fault signatures in successive attribute extraction steps. This fact can be appreciated from the observations of the co-rendered images of seismic attributes with amplitude data (Fig. 6a–d). Discontinuous structures are illuminated with low similarity values and variable dips (Fig. 6a and b). Higher dips are mainly observed towards the northern part of the prospect. Changes in dip (high to low) are observed in and around the fault zones. The upthrow portions of the discontinuous structures are effectively associated with higher positive curvature values (Fig. 6c). In the REF data, the features related to high similarity as well as artefacts have disappeared (compare Fig. 6a and d, parts marked with arrows and ovals). Thus, REF provides further improvement in the visualization of the fault or discontinuous zones compared to the similarity attribute alone (Fig. 6d and a). To further confirm this fact, these attributes are analysed in map view over the Wyandot Formation (Fig. 7a–b). The similarity attribute has revealed the major discontinuous structures within the formation but it is not efficient in deciphering minor discontinuities, as well as structural connectivity between them (Fig. 7a, parts in the ovals). However, REF has effectively revealed faults and discontinuities from the data and restored their

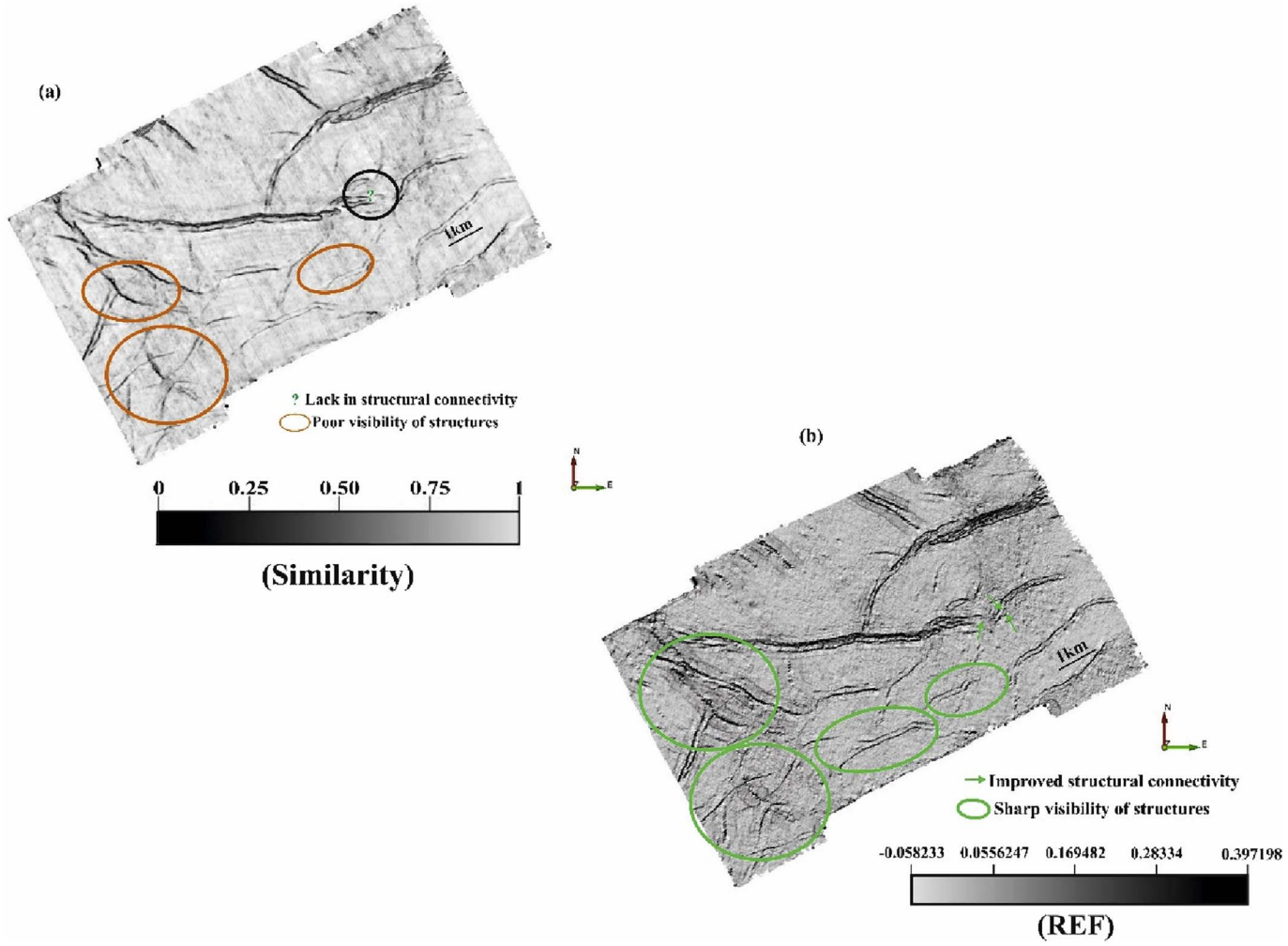

Fig. 7. (a) Similarity attribute computed using steering data is displayed over the Wyandot Formation. It illustrates a network of faults and discontinuities. These structural features are poorly visible (blurry appearance) in the SW and central portion (orange ovals) of the unit. Lack in structural connectivity is observed towards the eastern part of the unit and is indicated using black oval with a question mark. (b) REF computed using similarity attribute and FEF seismic is displayed over the Wyandot Formation top. Structural features are sharper and distinct in the SW and central portion of the unit (green oval) as compared to Fig. 7a. Moreover, the structural connectivity in the eastern part of the unit is now improved (green arrows). The REF acts as a balancing medium in improving structural images of geologic structures from the seismic data. (For interpretation of the references to colour in this figure legend, the reader is referred to the web version of this article.)

connectivity even when considering the minor discontinuities (Fig. 7b, see the parts as indicated by the ovals and arrows).

5.1. Neural analysis aiding structural interpretation

The multi-attribute analysis in this work demonstrates an increase in confidence when capturing detail structural characteristics within the Penobscot prospect. The neural training of the attributes based on the selected fault and non-fault locations (Fig. 8a), resulting in an enhanced fault probability attribute. Such training is carried out using a fully connected neural network that consists of 17 nodes; 10, 5, and 2 of which are related to the input, hidden and output layers, respectively (Fig. 8b). The 30% of the data were used for testing and 70% of the data were used for training during the neural computation. Iterative training was carried out such that weights get updated during the training phase. The relative contribution provided by each of the input unit is shown in Table 1. It is observed that after ten iterations the normalized root-mean-square (RMS) error curve for both test and train data sets achieve a minimum value lying between 0.4 and 0.5 (Fig. 8c). This has subsequently resulted in a minimum misclassification percentage of 3.46–5.57% (Fig. 8d) between the train and test data sets. The neural training finally resulted in a probability volume called as the fault probability cube (FPC) (Fig. 9), which captures and stores every minute structural disturbances that took place over a large geological time period, i.e. from the Jurassic to recent.

The FPC attribute has efficiently depicted the major fault and associated discontinuities within the Cretaceous units (i.e. LCF, DCF, and WF). The horizon maps as prepared over these units by co-rendering the FPC volume with similarity attribute have effectively delineated the shapes and trends of these discontinuities (Fig. 10a–c). The major fault illustrates NNW-SSE structural trend. Most of the interconnected discontinuous structures are clustered within the western part of the Cretaceous strata. It is also observed that the eastern part is structured with minor fault discontinuities. The major fault (F1) structurally divides the LCF into two major compartments: C1 (that lies over the downdip portion) and C2 (that lies over the updip portion) (Fig. 10a). However, the NE part of the formation within the updip portion is further compartmentalised by an EW trending fault (F2) into C3 and C4 compartments. Similar type of reservoir compartments are also developed within the DCF (Fig. 10b) and WF (Fig. 10c). Faulting has also resulted in relay ramp structures across all the three Cretaceous units. The SE portion of the WF is structured by several minor parallel faults that exhibit ~ EW structural trend. On the other hand, the SW part is associated with several interconnected fault networks. However, the underlying DCF and LCF are devoid of such structural complexities. Fault intersection zones are only observed in WF (Fig. 10c, within

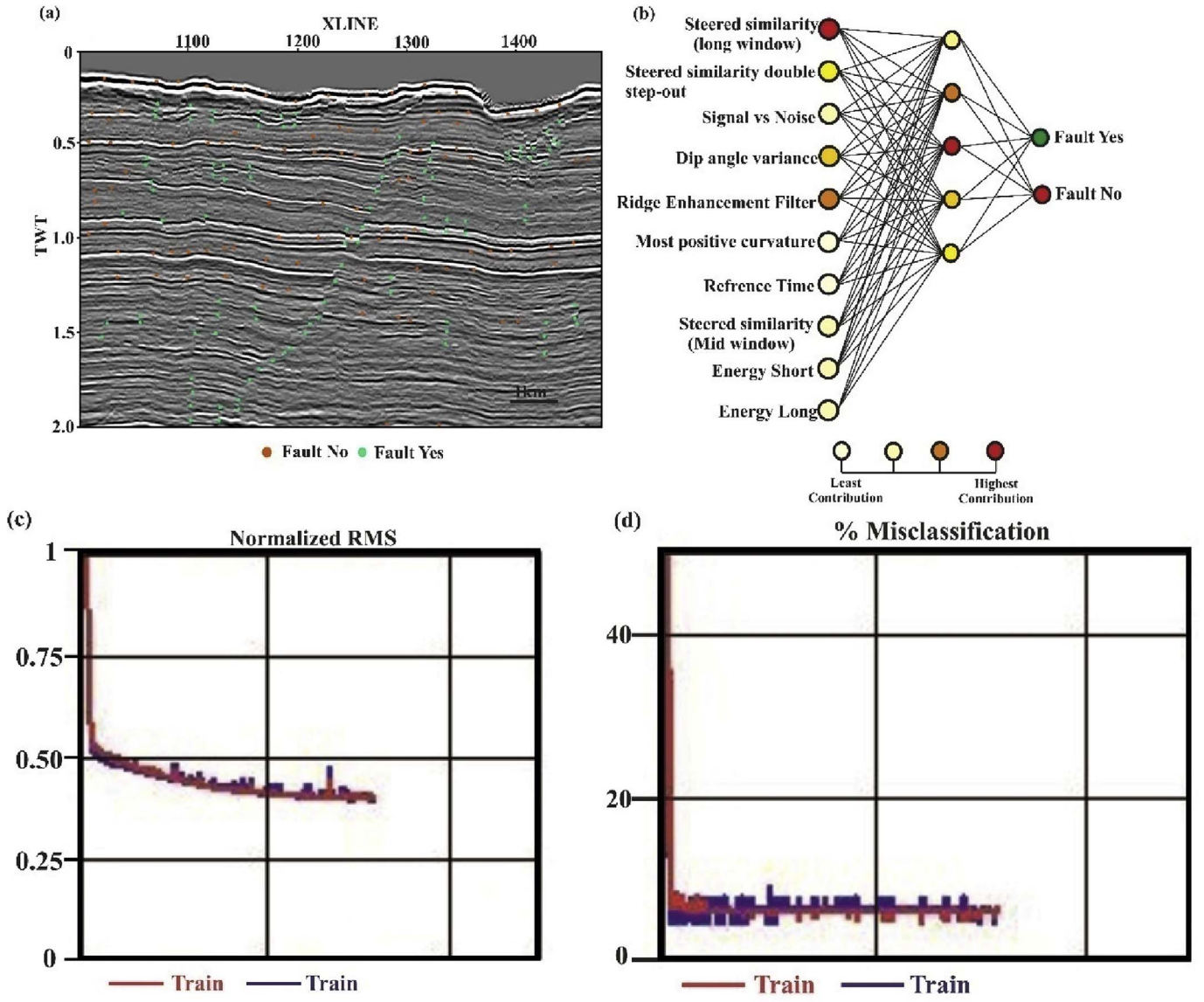

Fig. 8. (a) Example locations classified into fault-yes (green dots) and fault-no (red dots) groups, displayed for inline 1300. The MLP network gets trained over these example locations. (b) The MLP network consisting of three distinct layers: input layer (10 nodes), hidden layer (5 nodes) and output layer (2 nodes). Each layer is interconnected with each other through different nodes. The colour scale 'light yellow' to 'red' signifies the relative contribution of each input node to classify the output in terms of 'fault-yes' (green colour) and 'fault-no' (red colour). (c) Normalized RMS error between the test (seismic attributes) and trained (example locations) data sets. (d) Misclassification percentage of for test and trained data sets. (For interpretation of the references to colour in this figure legend, the reader is referred to the web version of this article.)

Table 1
Sensitivity chart showing the relative contribution of each attribute used for neural training.

ATTRIBUTES	WEIGHTS
Steered Similarity (Long Window)	96.4
Ridge Enhancement Filter	80.7
Dip Angle Variance	71.2
Steered Similarity Double Step-out	56.3
Steered Similarity (Mid Window)	34.5
Signal vs. Noise	27.3
Energy (Short)	22.2
Energy (Long)	17.8
Most Positive Curvature	11.2
Reference Time	4.7

ovals). Thus, WF has undergone severe episode of faulting when compared to the other two units. The major fault (F1) that cuts all of the three units illustrates straight shape with NNE-SSW trends, whereas the fault (F2) exhibits bow shape expression with EW trends.

5.2. Fault displacement study

The displacement-time profile of the major fault reveals different phases of fault growth with variable throws or vertical displacements over a large period of geologic time (the Jurassic through the Cretaceous to the Tertiary) (Fig. 11). During the Cretaceous, the Aptian-Cenomanian and the Cenomanian-Coniacian time periods recorded a cumulative throw of about 10.42 m and 18.21 m. Fault throw subsequently experienced a sudden increase (~51.79 m) from the Coniacian to Campanian. It further increased to about 79.33 m and continued within the Tertiary period. Such large throw build-up through different ages (geologic time) sheds light over the degree of tectonic activity and sediment loading-unloading phases of the basin.

Displacement-distance profiles (Fig. 12a–c) are computed to know the changes in throw values along the length of the major fault. This also helps in understanding the growth of the fault in spatial scale. The

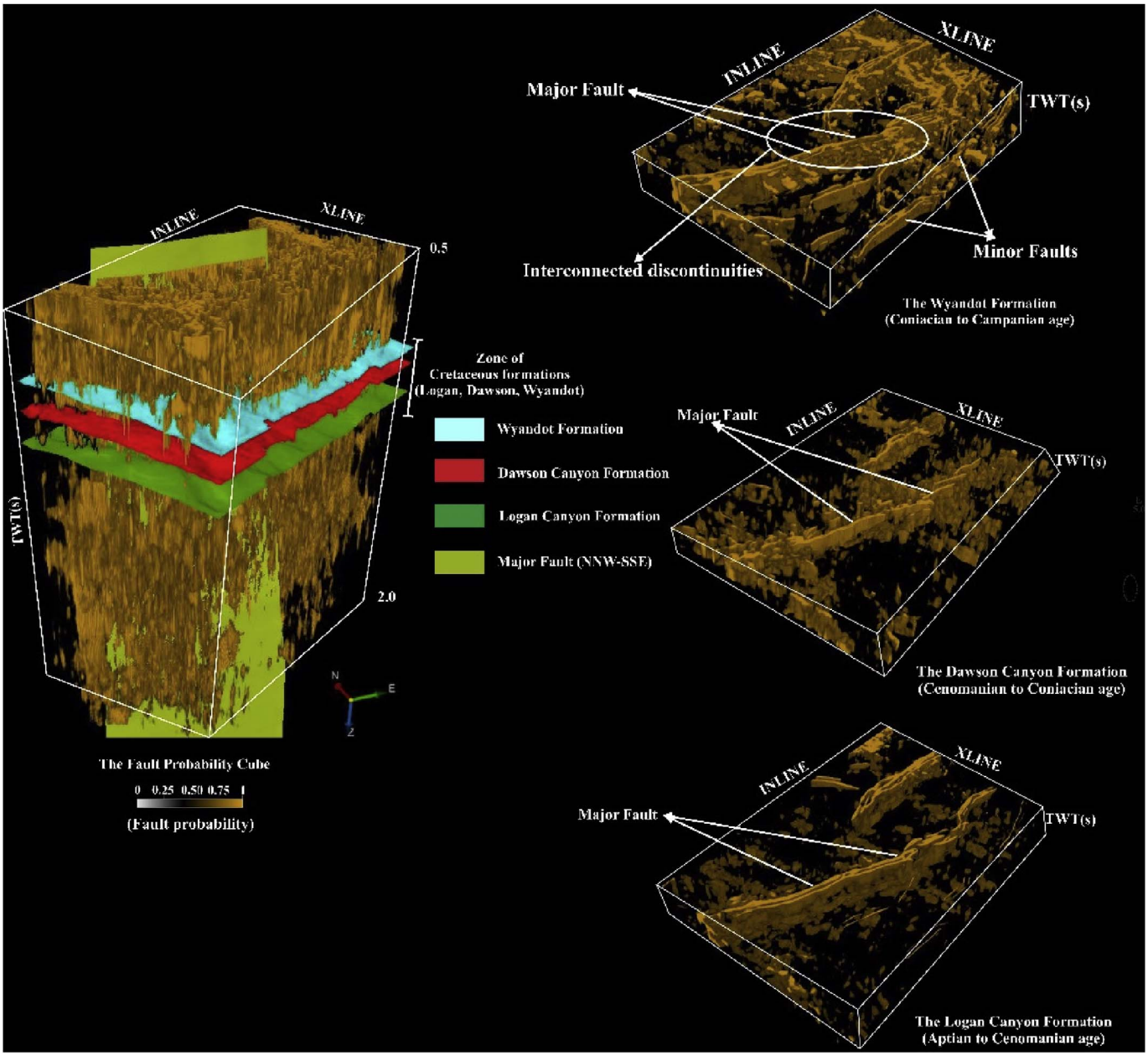

Fig. 9. 3D volumetric visualization of the fault probability cube (FPC) showing faults and discontinuity networks captured from the seismic data of the Penobscot prospect. Locations of the three Cretaceous units [i.e. the Wyandot (Blue), the Dawson Canyon (Red) and the Logan Canyon (Dark green) Formations] and the NNW-SSE trending major fault (Light green) are shown as coloured surfaces within the FPC. The FPC stores all minute structural details that have grown over the large geological time period. Several sub-volumes corresponding to the Cretaceous units are schematically displayed to appreciate effectiveness of the FPC in imaging minute details of the subsurface faults and discontinuities. (For interpretation of the references to colour in this figure legend, the reader is referred to the web version of this article.)

displacement-distance profile over the LCF demonstrates a bell-shaped pattern (Fig. 12a). It illustrates that the major fault suffers a smooth increment of throw or displacement (in the vertical dimension) in the western portion of the formation, with a sudden jump in displacement from ~20.42 m to 58.20 m at a distance of 500 m–625 m (Fig. 12a). The fault suffered a maximum displacement of 118.81 m at about 2.5 km distance along the strike. Moving further eastern part of the formation, fault displacement decreases and dies out (i.e. fault segment gets tapered off) at about 4.75 km along the strike direction. Maximum vertical displacement within the fault at about 2.5 km along the strike direction represents the core of the fault segments that coalesced over time to generate the fault. Within the DCF, the fault suffers a step-wise increment of displacement from western portion of the formation and encountered a sudden change in displacement from 18.86 m to 34.89 m at a distance of 750 m–875 m (Fig. 12b). At a distance of 3.25 km, the fault suffered a maximum displacement of 100.53 m. Displacement further continued and got tapered off at 4.75 km towards the eastern part of the unit. The overlying WF also experiences a gradual increment of displacement along the strike from western portion and encountered a sudden displacement of 49.11 m–79.11 m at a distance of 875 m to 1 km. At a distance of 3.25 km, the fault suffered a maximum displacement of 87.22 m. Displacement further continued and got tapered off at 4.75 km towards the eastern part of the formation (Fig. 12c).

6. Discussion

The Penobscot prospect within the Scotian Basin, demonstrates a

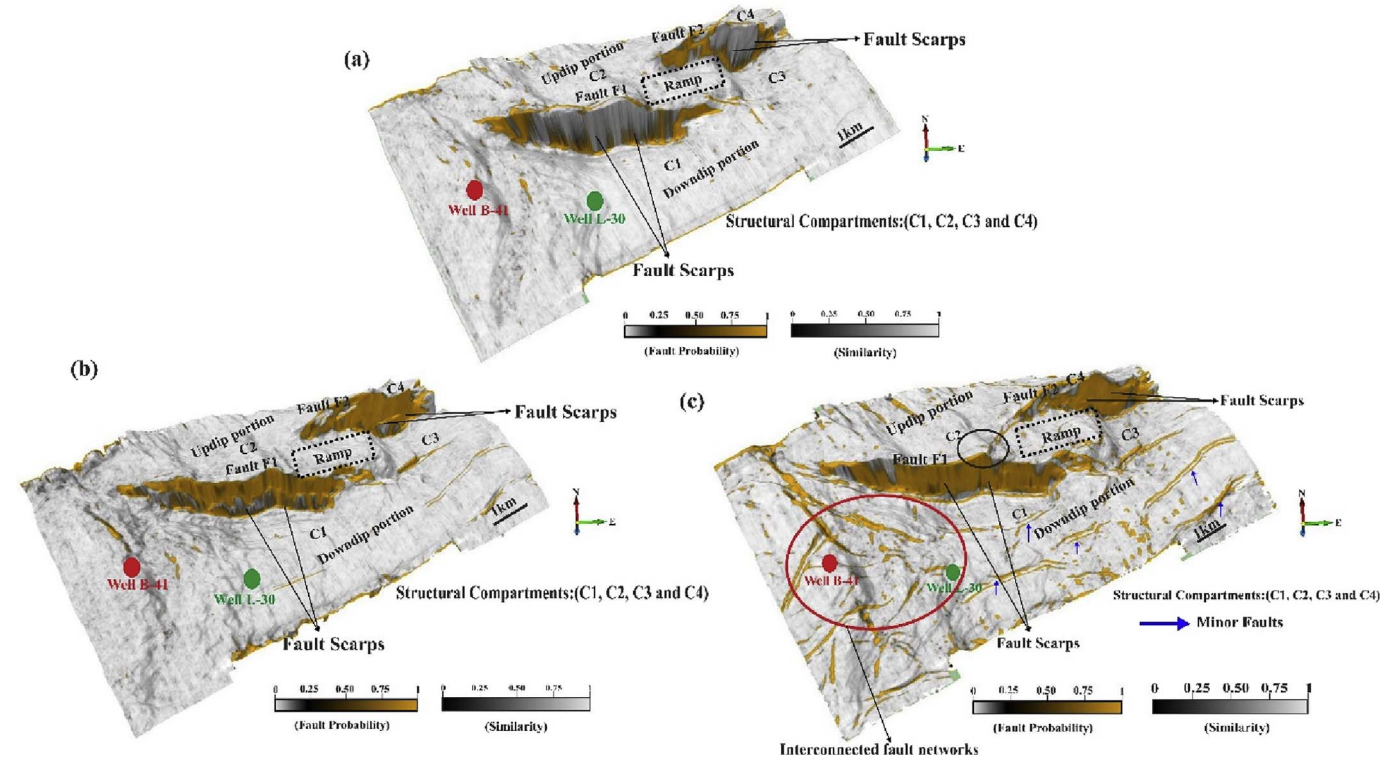

Fig. 10. FPC attribute co-rendered with the similarity attribute and displayed over the Cretaceous strata. Faults and discontinuities are associated with low similarity and high fault probability values. Faulting has resulted in relay ramp structures that are observed for all of the three Cretaceous units. (a) Logan Canyon Formation (LCF): Feeble structural compartments and faulting networks (also see Fig. 9) are observed within this unit. (b) Dawson Canyon Formation (DCF): Development of similar feeble structural compartments and faulting networks (also see Fig. 9) are also observed. (c) Wyandot Formation (WF): Intense structural compartments and faulting networks (red oval) are observed over this unit. The SE portion of the unit is associated with several minor faults that run parallel to each other. Fault intersections zones (black oval) are only observed within this unit. The Wyandot Formation reveals larger fault activities in comparison to the Logan Canyon and Dawson Canyon Formations. (For interpretation of the references to colour in this figure legend, the reader is referred to the web version of this article.)

large depositional history that ranges through the Jurassic, the Cretaceous, the Tertiary into the present day situation (Fig. 1c). The prospect has undergone several tectonic events and deformation scenario over this period. These deformations have resulted in the growth of several geo-tectonic features, e.g. faults, folds, fracture networks, etc., as well as varied degrees of sedimentation within the prospect. This resulted in different sediment thickness maps even within Cretaceous strata (Fig. 13a–c).

Yagci (2016) attempted to image the major fault and discontinuous features of the prospect using 2D seismic data through seismic attribute analysis. This work has delineated five minor faults and a major fault without inferring about the trend and continuity of these structural features, as well as their role in compartmentalization of the Cretaceous units. Most of the literature (Kettanah, 2013; Qayyum et al., 2015) highlights the evolution and depositional histories of the older units belonging to the Triassic and Jurassic periods. However, no work has

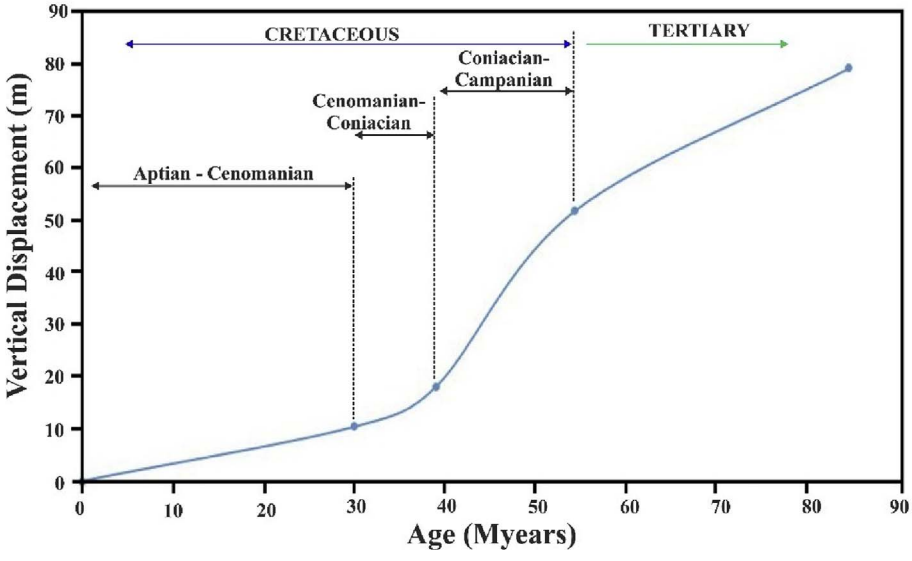

Fig. 11. Cumulative vertical displacements of the geologic strata (Cretaceous to Tertiary) with respect to geologic age (M years). The plot illustrates a steady growth of the fault over the Cretaceous to the Tertiary time period.

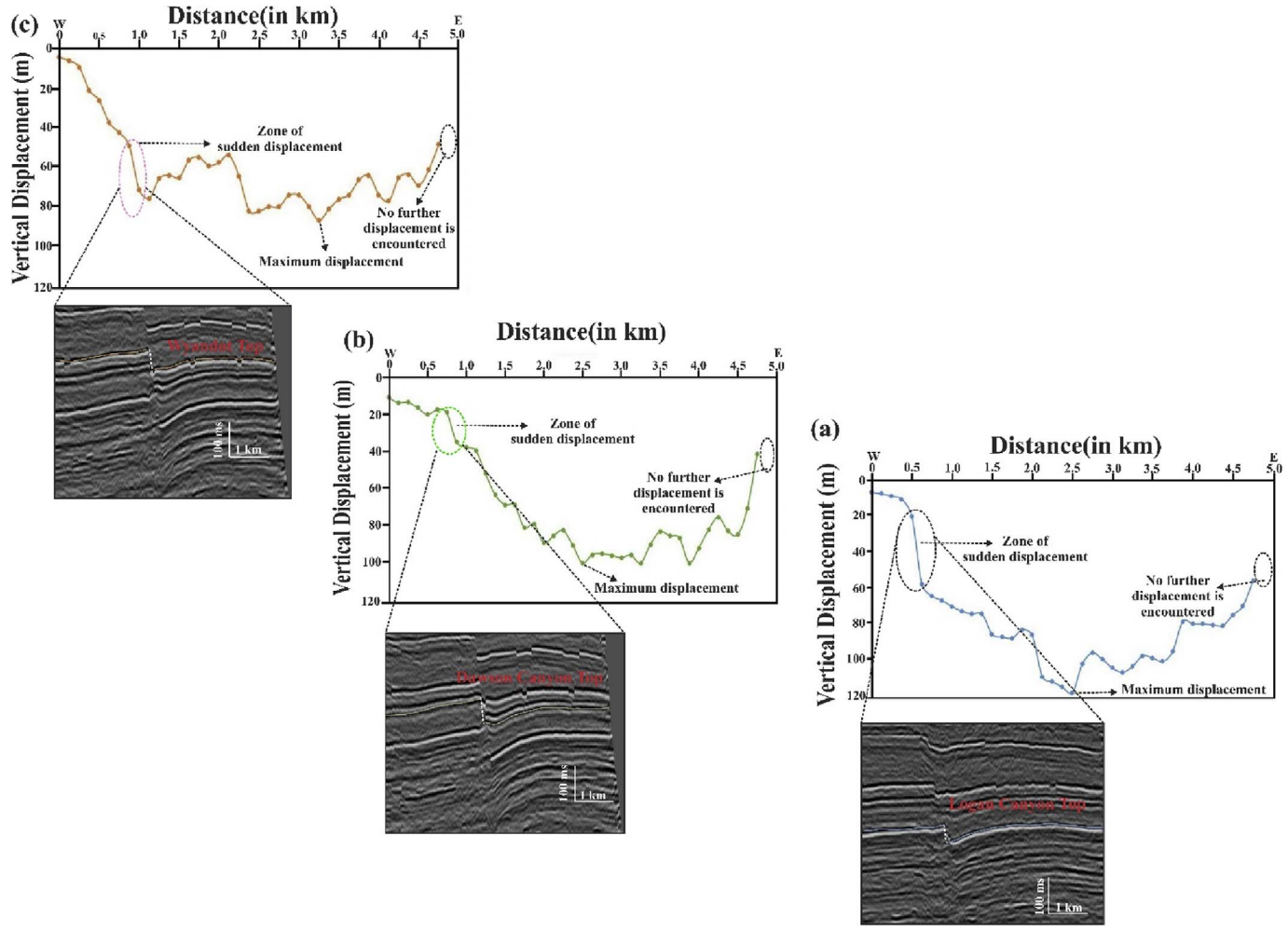

Fig. 12. Displacement-distance profiles for the three strata deposited during the Cretaceous period. (a) Logan Canyon Formation (LCF): Zone of sudden displacement is indicated using black dotted oval. Such displacement is illustrated using the corresponding zoomed part of the seismic section. Maximum vertical displacement of 118.81 m is observed at a distance of 2.5 km. (b) Dawson Canyon Formation (DCF): A zone of sudden displacement is indicated using light green dotted oval. Such a displacement is also illustrated using the corresponding zoomed part of the seismic section. Maximum vertical displacement of 100.3 m is observed at a distance of 3.25 km. (c) Wyandot Formation (WF): A zone of sudden displacement is indicated using pink dotted oval. Such displacement is illustrated using the corresponding zoomed part of the seismic section. Maximum vertical displacement of 87.22 m is observed at a distance of 3.25 km. (For interpretation of the references to colour in this figure legend, the reader is referred to the web version of this article.)

been done to understand the role of younger units (Cretaceous to Tertiary) in controlling and shaping the subsurface of the Penobscot prospect. Campbell et al. (2015) provide a reliable documentation to such objective, where the authors provided lithological compositions to the overlying Cretaceous units. They inferred that the LCF is composed of sand beds inter-fingered with shale packages; the DCF is a shaley unit and contributes to be a source as well as an appropriate seal; and the younger WF consists large amount of chalk deposits giving rise to accumulation of good amount of hydrocarbon deposits. Similar Cretaceous units are hydrocarbon producing zones at the adjacent of the Penobscot prospect in the Deep Panuke project (since 2013). However, wells in the Penobscot prospect, L-30 and B-41 did not show such evidence of hydrocarbon. Well B-41 proved to be a dry well, whereas evidence of feeble amounts of hydrocarbons was observed at L-30. These contradicting scenarios also evoke us to take up this work to understand the factors that may have caused the complex nature of the study area.

In the present study, the geostatistical filtering (based on factorial kriging technique) proves to be very efficient in removing footprints related noise (Fig. 3a–b). The steering cube computation, followed by structural filtering of this noise free data (Figs. 3b and 4a) has significantly improved the visibility as well as continuity of the faults and structural features in the interpreted data (Fig. 4c). Thus, the present workflow not only demonstrates a robust data conditioning approach for enhanced structural interpretation but also provides better input for attribute computation. In this work, faults and other structural discontinuities are visualized first through this advanced data conditioning approach and then through several attribute computations as well as multi-attribute analyses using ANN. This also helps understanding the degree of relative tectonic activity and structural complexity between the three Cretaceous units. Utilising these enhanced fault image, in the second part of the work, the fault displacement study has been carried out to provide a comprehensive understanding of the growth and evolution of the major fault as well as that of the related Cretaceous units. The ANN technique adds value to such interpretation strategy by generating the FPC volume that improves the structural detailing of the subsurface (in general) and the Cretaceous units in particular (Fig. 9). Analyses of fault displacement profiles (Figs. 11 and 12a-12c) have effectively brought out the growth history of the major fault with time and space as well as opined on its impact in deforming the Cretaceous units. It is observed that the major fault system has not only compartmentalised the entire prospect but also exhibited an important contribution in deforming different geologic strata within the basin. During the Aptian to Cenomanian age, the fault system had severe impact over the LCF, thereby, causing it to displace about ~118.81 m in a vertical direction. Though the overlying DCF and WF are also deformed by

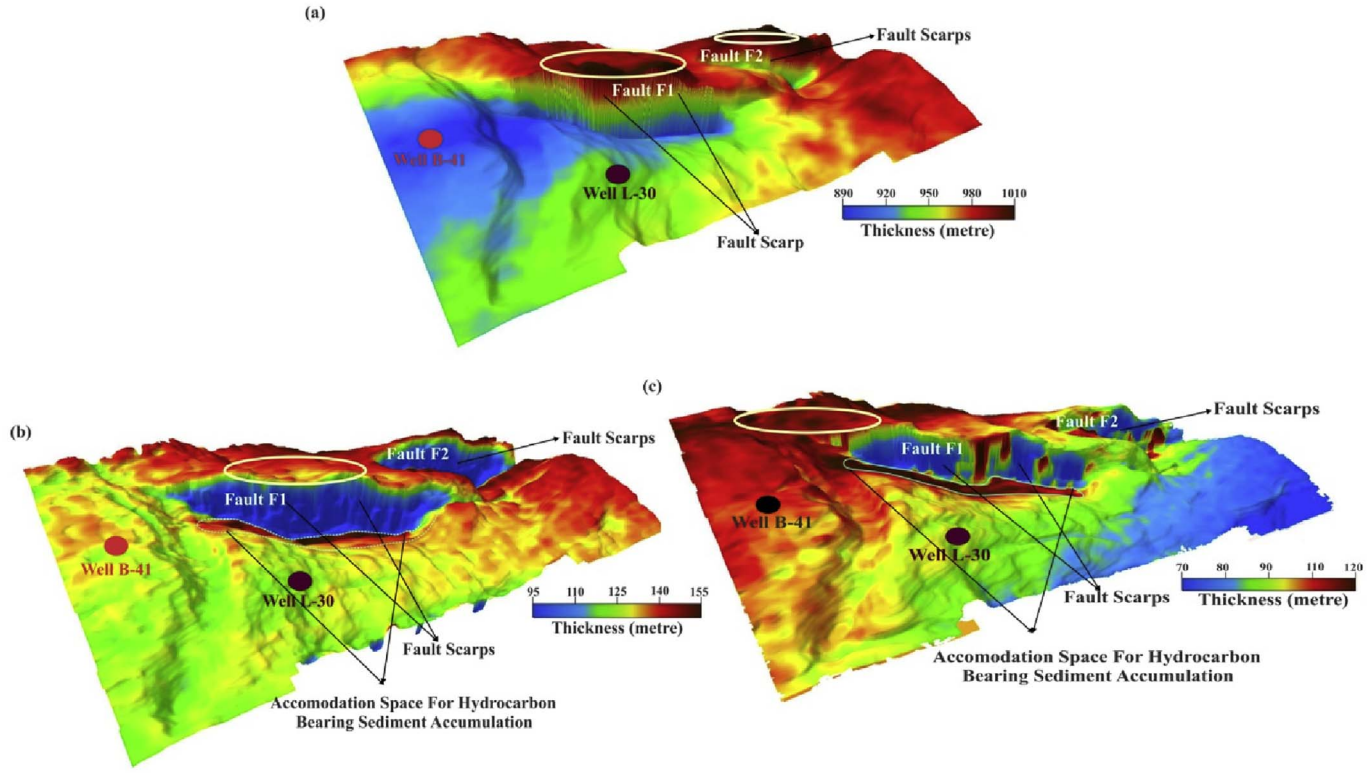

Fig. 13. Thickness map for the three strata deposited during the Cretaceous period. (a) Sediment thickness of the Logan Canyon Formation (LCF). Zone of thick deposition of sediments in this map are located over the fault F1 and F2 (yellow oval). (b) Sediment thickness of Dawson Canyon Formation (DCF). It has also experienced similar depositional process around the fault, i.e. on both side of the fault, updip (light yellow oval) and downdip (dotted lines) portions. (c) Sediment thickness of Wyandot Formation (WF). WF regarded as the reservoir rock (Campbell et al., 2015) and has the thickest deposition of sediments in the updip part (light yellow oval) and also in the downdip portion of the major fault, just adjacent to the fault scarp (dotted lines). The drilled wells, B-41 and L-30 are just away from the large deposition areas and faulted zones. This provides significant clues on the failure of the two wells shown in the figure. (For interpretation of the references to colour in this figure legend, the reader is referred to the web version of this article.)

faulting, the WF encountered smaller vertical displacements as compared to the underlying DCF and LCF. Such faulting scenario have also given rise to the development of several other geologic structures (e.g. minor faults, fracture networks, folds) within the WF, making it structurally more complicated in comparison to the underlying strata. This may have led to the development of bigger chain of structural discontinuities in WF (Fig. 10c). Thus, the inferences related to the degree of faulting activities and structural complexities of the Cretaceous units as given from the FPC volume (see section '5.1. Neural analysis aiding structural interpretation') are also validated by the observations from the fault displacement study.

These structural discontinuities within the Cretaceous units might have led to the development of accommodation space for the deposition of hydrocarbon bearing sediment or they might have acted as trap closures (Fig. 10a–c and 13a-13c). The thickness maps also depict the presence of thick sediment deposition around the fault F1 and F2 of the study area (Fig. 13a–c). These observations allow us to think that the faulted areas within these units could be the better plausible zones of hydrocarbon accumulation. Thus, the structural architecture of the geologic strata as well as the major fault system (that divides the prospect) might have played a significant role in deforming and undulating these geologic strata. This not only resulted as major entrapment zones, but also exhibited leaking nature to provide conducive pathways for the accumulated hydrocarbon bearing sediments to migrate from drilled wells to other locations. This might have caused the failure of the existing wells (B-41, and L-30). Thus, the present interpretation strategies have brought out a newer dimension into the understanding of the structural complexities of the prospect and provides significant inputs for the future exploration programme of the Penobscot prospect.

7. Conclusions

The Penobscot prospect is structurally characterized by several geotectonic features that modulate the subsurface. Interpretation of these features is a challenging task but success of the present interpretation strategy aids in understanding the structural architecture of the complex geologic strata. The present study throws light on such facts and delivers an enhanced structural interpretation of Cretaceous units in the Penobscot prospect. Improved conditioning of seismic data, and extraction of various structural attributes, as well as hybrid attributes through neural computation, have been very effective in capturing the detailed structural variations within the Cretaceous units of the study area. The present fault displacement studies of the major fault confirm the existence of high degree of structural activities within WF in comparison to the other Cretaceous units of the basin. This major fault is the integration of several fault segments generated over time, and has yielded number of depositional compartments and closures for the hydrocarbon bearing sediments of the prospect. However, we feel that additional studies such as detail reservoir modelling and characterizing the petro-physical properties of these geologic strata would help in drawing out rigorous inferences regarding the exploration and exploitation activities within the prospect.

Acknowledgements

Thanks are due to dGB Earth Sciences™ for providing academic licence of OpendTect™ (v6.0.7) software to the Department of Earth Sciences, Indian Institute of Technology Kanpur, India. Canada-Nova Scotia Offshore Petroleum Board (CNSOPB) is acknowledged for providing the 3D seismic and well data sets for carrying out this research. We would also like to thank Associate Editor Tiago Alves, reviewers

David Iacopini and Haibin Di for their constructive criticism and suggestions that helped to improve the manuscript.

References

Albertz, M., Beaumont, C., 2010. An investigation of salt tectonic structural styles in the Scotian Basin, offshore Atlantic Canada: 2. Comparison of observations with geometrically complex numeral models. Tectonics 29 TC4018.

Albertz, M., Beaumont, C., Shimeld, J.W., Ings, S.J., Gradmann, S., 2010. An investigation of salt tectonic structural styles in the Scotian Basin, offshore Atlantic Canada: 1, Comparison of observations with geometrically simple numerical models. Tectonics 29 TC4017.

Al-Dossary, S., Marfurt, K.J., 2006. 3-D volumetric multi-spectral estimates of reflector curvature and rotation. Geophysics 71, 41–51.

Alves, T.M., Omosanya, K., Gowling, P., 2015. Volume rendering of enigmatic high-amplitude anomalies in southeast Brazil: a workflow to distinguish lithologic features from fluid accumulations. Interpretation 3 (2), A1–A14.

Atakulreka, A., Sutivong, D., 2007. Avoiding local minima in feed forward neural networks by simultaneous learning, paper presented at 20th Australian Joint Conference on Artificial Intelligence.

Avseth, P., Mukerji, T., Mavko, G., 2005. Quantitative Seismic Interpretation: Applying Rock Physics Tools to Reduce Interpretation Risk. Cambridge Univ. Press, pp. 409.

Bahorich, M., Farmer, S., 1995. 3-D seismic discontinuity for faults and stratigraphic features: the coherence cube. Lead. Edge 14, 1053–1058.

Campbell, T.J., Richards, F.W.B., Silva, R.L., Wach, G., Eliuk, L., 2015. Interpretation of the Penobscot 3D seismic volume using constrained sparse spike inversion, Sable sub-Basin, offshore Nova Scotia. Mar. Petroleum Geol. 68, 73–93.

Chehrazi, A., Rahimpour-Bonab, H., Rezaee, M., 2013. Seismic data conditioning and neural network-based attribute selection for enhanced fault detection. Pet. Geosci. 19 (2), 169–183.

Chopra, S., Marfurt, K.J., 2007a. Seismic Attributes for Prospect Identification and Reservoir Characterization. SEG, Tulsa.

Chopra, S., Marfurt, K.J., 2007b. Curvature attribute applications to 3D surface seismic data. Lead. Edge 26 (4), 404–414.

Canada-Nova Scotia Offshore Petroleum Board (CNSOPB), 2008. Call for bids 2008–2009 NS08-2, Sub-regional geology. www.cnsopb.ns.ca/call_for_bids_08_2/cnsopb/subregional_geology.html.

Cohen, I., Coult, N., Vassiliou, A.A., 2006. Detection and extraction of fault surfaces in 3D seismic data. Geophysics 71 (4), P21–P27.

Di, H., Gao, D., 2017. 3D seismic flexure analysis for subsurface fault detection and fracture characterization. Pure Appl. Geophys. 174, 747–761.

Fehmers, G.C., Höcker, C.F.W., 2003. Fast structural interpretation with structure-oriented filtering. Geophysics 68 (4), 1286–1293.

Fensome, R.A., Crux, J.A., Gard, I.G., MacRae, R.A., Williams, G.L., Thomas, F.C., Fiorini, F., Wach, G., 2008. The last 100 million years on the Scotian Margin, offshore eastern Canada: an event-stratigraphic scheme emphasizing bio-stratigraphic data. Atl. Geol. 44, 93–126.

Grist, A.M., Reynolds, P.H., Zentilli, M., Beaumont, C., 1992. The Scotian Basin offshore Nova Scotia: thermal history and provenance of sandstones from apatite fission track and 40Ar/39Ar data. Can. J. Earth Sci. 29 (5), 909–924.

Hale, D., 2013. Methods to compute fault images, extract fault surfaces, and estimate fault throws from 3D seismic images. Geophysics 78, O33–O43.

Iacopini, D., Butler, R.W.H., Purves, S., McArdle, N., Freslon, N.D., 2016. Exploring the seismic expression of fault zones in 3D seismic volumes. J. Struct. Geol. 89, 54–73.

Jansa, L. F., Wade, J. A., 1975. Geology of continental margin off Nova Scotia and Newfoundland, Offshore Geology of eastern Canada, Regional Geology, vol. 2. Geological Survey of Canada (74–30), 51–106.

Kettanah, Y.A., 2013. Hydrocarbon fluid inclusions in the Argo salt, offshore Canadian Atlantic margin1. Can. J. Earth Sci. 50 (6), 607–635.

King, L.H., MacLean, B., Fader, G.B., 1974. Unconformities on the Scotian Shelf. Can. J. Earth Sci. 11 (1), 89–100.

Kumar, P. C., 2016. Application of geometric attributes for interpreting faults from seismic data: an example from Taranaki Basin, New Zealand. SEG Technical Program Expanded Abstracts, 2077–2081.

Kumar, C.P., Mandal, A., 2017. Enhancement of fault interpretation using multi-attribute analysis and artificial neural network (ANN) approach: a case study from Taranaki Basin, New Zealand (Online Early). Explor. Geophys Article number: EG16072. https://doi.org/10.1071/EG16072.

Ligtenberg, J.H., Wansink, A.G., 2001. Neural network prediction of permeability in the El Garia Formation, Ashtart oilfield, offshore Tunisia. J. Petroleum Geol. 24, 389–404.

Liu, Y., Liu, C., Wang, D., 2008. A 1D time varying median filter for seismic random, spike-like noise elimination. Geophysics 74 (1) V17–V24.

Magneron, C., Petit, F., 2008. M-GS - new spatial estimation and simulation models for more Precision and more realism. 70th EAGE Conference and exhibition incorporating SPE EUROPEC 2008, extended Abstract, doi: 10.3997/2214-4609.20147579.

Magneron, C., Bourges, M., Jeannee, N., 2009. M-Factorial Kriging for Seismic Data Noise Attenuation. 11th International Congress of the Brazilian Geophysical Society & EXPOGEF 2009, Salvador, Bahia, Brazil, 1651–1654. https://doi.org/10.1190/sbgf2009-347.

Marfurt, K.J., Alves, T.M., 2015. Pitfalls and limitations in seismic attribute interpretation of tectonic features. Interpretation 3 (1) SB5–SB15.

McCormack, M.D., 1991. Neural computing in geophysics. Lead. Edge 10 (1), 11–15.

McIver, N.L., 1972. Cenozoic and Mesozoic stratigraphy of the Nova Scotia Shelf. Can. J. Earth Sci. 9, 54–70.

McLeod, A.E., Dawers, N.H., Underhill, J.R., 2000. The propagation and linkage of normal faults: insights from the Strathspey–Brent–Statfjord fault array, northern North Sea. Basin Res. 12, 263–284. http://dx.doi.org/10.1111/j.1365-2117.2000.00124.x.

Meldahl P., Heggland, R., Bril, A.H., de Groot, P., 1999. The chimney cube, an example of semi-automated detection of seismic objects by directive attributes and neural networks: Part I; methodology. SEG Technical Program Expanded Abstracts, 931–934.

Piazza, J.L., Magneron, C., Demongin, T., Muller, N.A., 2015. M-Factorial Kriging - An Efficient Aid to Noisy Seismic Data Interpretation. Petroleum Geostatistics 2015, Extended Abstract, doi: http://dx.doi.org/10.3997/2214-4609.201413594.

Qayyum, F., Catuneanu, O., Bouanga, C.E., 2015. Sequence stratigraphy of a mixed siliciclastic-carbonate setting, Scotian Shelf, Canada. Interpretation 3, 21–37.

Raya, P. Y., Li, X. P., 2008. The factorial kriging technique: A geostatistical tool for acquisition footprints removal — A case study. SEG Technical Program Expanded Abstracts, 2657–2661. https://doi.org/10.1190/1.3063895.

Roberts, A., 2001. Curvature attributes and their application to 3D interpreted horizons. First break 19, 85–100.

Singh, D., Kumar, P.C., Sain, K., 2016. Interpretation of gas chimney from seismic data using artificial neural network: a study from Maari 3D prospect in the Taranaki Basin, New Zealand. J. Nat. Gas Sci. Eng. 36, 339–357.

Smith, T., Treitel, S., 2010. Self-organizing artificial neural nets for automatic anomaly identification. SEG Technical Program Expanded Abstracts, 1403–1407.

Tingdahl, K.M., 1999. Improving Seismic Detectability Using Intrinsic Directionality. Technical Report. Earth Sciences Centre, Gotenborg University, pp. B194.

Tingdahl, K.M., Bril, A.H., de Groot, P., 2001. Improving Seismic chimney detection using directional attributes. J. Petroleum Sci. Eng. 29, 205–211.

Tingdahl, K.M., 2003. In: Nikarvesh, M., Aminzadeh, F., Zadeh, L.A. (Eds.), Improving Seismic Chimney Detection Using Directional Attributes in Soft Computing and Intelligent Data Analysis in Oil Exploration. Developments in Petroleum Science, 51. Elsevier Science Publishers, Amsterdam, pp. 157–173.

Tingdahl, K.M., de Groot, P., 2003. Post-stack dip- and azimuth processing. J. Seismic Explor. 12,113–126.

Tingdahl, K.M., de Rooij, M., 2005. Semi-automatic detection of faults in 3D seismic data. Geophys. Prospect. 53 (4), 533–542.

Wade, J.A., Maclean, B.C., Williams, G.L., 1995. Mesozoic and Cenozoic stratigraphy, eastern Scotian Shelf: new interpretations. Can. J. Earth Sci. 32, 1462–1473.

Wade, J.A., MacLean, B.C., 1990. Aspects of the geology of the Scotian Basin from recent seismic and well data: geology of the continental margin of eastern Canada. Geological Survey of Canada. Geol. Can. 2, 190–238.

Walsh, J.J., Nicol, A., Childs, C., 2002. An alternative model for the growth of faults. J. Struct. Geol. 24 (11), 1669–1675.

Weickert, J., 1999. Coherence-enhancing diffusion filtering. Int. J. Comput. Vis. 31, 111–127.

Yagci, F.G., 2016. Reprocessing and Structural Interpretation of Multichannel Seismic Reflection Data from Penobscot, Nova Scotia. M.S. thesis, Paper 7528. Missouri Uni. Sci. Techno, U.S.A.

Zheng, Z., Kavousi, P., Di, H., 2014. Multi-attributes and neural network-based fault detection in 3D seismic interpretation. Adv. Mater. Res. 838–841, 1497–1502.